

## Article

# Na<sub>4</sub>Fe<sub>3</sub>(PO<sub>4</sub>)<sub>2</sub>(P<sub>2</sub>O<sub>7</sub>)@C/Ti<sub>3</sub>C<sub>2</sub>T<sub>x</sub> Hybrid Cathode Materials with Enhanced Performances for Sodium-Ion Batteries

Ao Xiang <sup>1</sup>, Deyou Shi <sup>2</sup>, Peng Chen <sup>2</sup>, Zhongjun Li <sup>2</sup>, Quan Tu <sup>2</sup>, Dahui Liu <sup>1</sup>, Xiangguang Zhang <sup>1</sup>, Jun Lu <sup>1</sup>, Yan Jiang <sup>1</sup>, Ze Yang <sup>3,\*</sup> and Pei Hu <sup>1,\*</sup>

<sup>1</sup> School of Science, Hubei University of Technology, Wuhan 430068, China; 102112283@hbust.edu.cn (A.X.); fttr@hbust.edu.cn (D.L.); 102102236@hbust.edu.cn (X.Z.); 102112271@hbust.edu.cn (J.L.); yanjiang@hbust.edu.cn (Y.J.)

<sup>2</sup> Wuhan Qina New Energy Technology Co., Ltd., Wuhan 430068, China; shideyou@qinaxinnengyuan.com (D.S.); chenpeng@qinaxinnengyuan.com (P.C.); lizhongjun@qinaxinnengyuan.com (Z.L.); tuquan@qinaxinnengyuan.com (Q.T.)

<sup>3</sup> Institute of Nanoscience and Nanotechnology, College of Physical Science and Technology, Central China Normal University, Wuhan 430079, China

\* Correspondence: yz@ccnu.edu.cn (Z.Y.); hupei@hbust.edu.cn (P.H.)

**Abstract:** Developing cost-effective cathode materials is conducive to accelerating the commercialization of sodium-ion batteries. Na<sub>4</sub>Fe<sub>3</sub>(PO<sub>4</sub>)<sub>2</sub>P<sub>2</sub>O<sub>7</sub> (NFPP) has attracted extensive attention owing to its high theoretical capacity, stable structure, and low cost of raw materials. However, its inherent low conductivity hinders its further application. Herein, carbon-coated NFPP nanospheres are anchored to crumpled MXene nanosheets by an electrostatic self-assembly; this cross-linked structure induced by CTAB not only significantly expands the contact area between particles and improves the electronic conductivity, but also effectively reduces the aggregation of NFPP nanoparticles. The as-designed Na<sub>4</sub>Fe<sub>3</sub>(PO<sub>4</sub>)<sub>2</sub>(P<sub>2</sub>O<sub>7</sub>)@C/Ti<sub>3</sub>C<sub>2</sub>T<sub>x</sub> (NFPP@MX) cathode exhibits a high discharge capacity (106.1 mAh g<sup>-1</sup> g at 0.2 C), good rate capability (60.4 mAh g<sup>-1</sup> at 10 C), and a long-life cyclic stability (85.2% capacity retention after 1000 cycles at 1 C). This study provides an effective strategy for the massive production of high-performance NFPP cathodes and broadens the application of MXene in the modification of other cathode materials.



**Citation:** Xiang, A.; Shi, D.; Chen, P.; Li, Z.; Tu, Q.; Liu, D.; Zhang, X.; Lu, J.; Jiang, Y.; Yang, Z.; et al.

Na<sub>4</sub>Fe<sub>3</sub>(PO<sub>4</sub>)<sub>2</sub>(P<sub>2</sub>O<sub>7</sub>)@C/Ti<sub>3</sub>C<sub>2</sub>T<sub>x</sub>  
Hybrid Cathode Materials with  
Enhanced Performances for  
Sodium-Ion Batteries. *Batteries* **2024**,  
10, 121. <https://doi.org/10.3390/batteries10040121>

Academic Editor: A. Robert Armstrong

Received: 5 March 2024

Revised: 22 March 2024

Accepted: 30 March 2024

Published: 3 April 2024



**Copyright:** © 2024 by the authors. Licensee MDPI, Basel, Switzerland. This article is an open access article distributed under the terms and conditions of the Creative Commons Attribution (CC BY) license (<https://creativecommons.org/licenses/by/4.0/>).

## 1. Introduction

Solar and wind are experiencing a boom to replace fossil energy which produces large amounts of carbon emissions. The volatility and unpredictability of renewable energy poses a huge challenge to grid stability; developing large-scale energy storage systems is essential to achieve a reliable and robust sustainable energy system [1,2]. Lithium-ion battery (LIB) technology achieved commercial success in powered vehicles and provides respectable energy densities, but the scarcity of lithium resources and a highly concentrated supply chain have led to an unstable market, which, coupled with increasing demand, has caused the cost of lithium to skyrocket. This is not optimistic for building cost-effective energy storage systems on a large scale [3–5]. Sodium-ion batteries are considered a competitive alternative to address the inherent limitations of lithium in terms of sustainability due to abundant economic sodium resources, reduced collector costs, and intercalation chemistry like LIB [6,7]. Compared to lithium ions (0.76 Å), Na ions (1.02 Å) with larger radii require a more open and stable frame structure to accommodate ion intercalation/extraction [8–10].

Hard carbon can achieve a reversible capacity over 300 mAh g<sup>-1</sup>, which has been proven to meet the practical application of SIBs. Therefore, the performance of SIBs is mainly limited by the cathode materials. To date, scholars have investigated various cathode materials for SIBs, such as sodium transition metal oxides [11–13], Prussian blue

analogues [14–16], and polyanionic compounds [17–20]. Transition metal oxides have a lack of stability owing to the intricate reaction involved in the phase transition during uninterrupted  $\text{Na}^+$  ion insertion/extraction. Moreover, they are highly hygroscopic, requiring harsh environments for electrode preparation, which inevitably increases costs [21]. The electrochemical properties of Prussian blue analogues are greatly affected by defects and crystal water content, and they are difficult to synthesize in large-scale stationary production [22].

Compared with the above two compounds, polyanionic compounds exhibit a stable 3D structural framework, good stability in air, and large-scale production. The exploration of polyanionic compounds has been basically focused on V- and Fe-based compounds. V-based compounds such as  $\text{Na}_3\text{V}_2(\text{PO}_4)_3$  [23,24] and  $\text{Na}_7\text{V}_4(\text{P}_2\text{O}_7)_4\text{PO}_4$  [25] exhibit impressively high operating voltages and high energy densities, but the high cost and toxicity of the V element should not be ignored. Polyanions with iron as the redox center seem to be the most ideal choice for electrode materials. Recently,  $\text{Na}_4\text{Fe}_3(\text{PO}_4)_2(\text{P}_2\text{O}_7)$  (denoted as NFPP) was screened from a variety of framework materials [26,27]. It has mild theoretical capacity of  $128.9 \text{ mAh g}^{-1}$  and high average operating voltage of 3.1 V. In addition, the dimer of the  $\text{PO}_4$  and  $\text{P}_2\text{O}_7$  groups in its structure provides a stable interstitial space and the volume change is less than 4% during the reversible extraction/insertion of three sodium ions [28,29]. Kang et al. first synthesized NFPP particles via a simple solid-state method using phosphate and pyrophosphate as raw materials, and revealed that it has excellent ion storage capabilities [30]. Yang et al. fabricated carbon-coated NFPP by thermal conversion of  $\text{PO}_4$  to  $\text{P}_2\text{O}_7$  using the sol-gel method [31]. However, NFPP suffers from intrinsic low electronic conductivity, which significantly limits its electrochemical performance. Constructing a firm 3D conductive structure to facilitate redox reactions of NFPP remains an important research subject [32,33].

MXene is a family of 2D transition metal carbides and/or nitrides. It is prepared by etching the intermediate A atomic layer from the ternary layered compound MAX. The general formula is  $\text{M}_{n+1}\text{X}_n\text{T}_x$ , where M denotes early transition metals, X corresponds to C or/and N, and  $\text{T}_x$  represents surface terminations [34]. Among them,  $\text{Ti}_3\text{C}_2\text{T}_x$  has been widely studied due to its mature synthesis technology, excellent electronic conductivity, robust mechanical properties, and strong interfacial coupling [35,36]. In previous reports, MXene has also been incorporated into the cathode material of SIBs [37]. Cao et al. prepared a heterostructure  $\text{Na}_3\text{V}_2\text{O}_2(\text{PO}_4)_2\text{F}/\text{Ti}_3\text{C}_2\text{T}_x$ , in which  $\text{Ti}_3\text{C}_2\text{T}_x$  nanosheets were used as mechanical scaffolds to inhibit the aggregation of  $\text{Na}_3\text{V}_2\text{O}_2(\text{PO}_4)_2\text{F}$  NPs and significantly improve the cyclic stability of electrodes [38]. Feng et al. fabricated an  $\text{NaFeFe}(\text{CN})_6/\text{MXene}$  flexible self-supporting electrode.  $\text{Ti}_3\text{C}_2\text{T}_x$  increases the electrical conductivity of nano-PBAs, and acts as a flexible matrix, which effectively reduces the expansion of flexible electrodes [39]. Nevertheless, in these cross-stacked structures, the contact area between particles is finite, and the “buffering effect” of MXene remains be optimized.

In this work, NFPP@MX composite was prepared by an electrostatic self-assembly method. In this composite, homogenous NFPP@C nanospheres are anchored to crumpled MXene nanosheet scaffolding. This tightly cross-linked structure not only significantly expands the contact area between particles and provides “superhighways” for fast electron transport, but also restricts the aggregation of NFPP@C particles thereby guaranteeing fast ion transportation. The resulting NFPP@MX electrode exhibits a high reversible capacity of  $106.1 \text{ mAh g}^{-1}$  at 0.2 C, a good rate capability ( $60.4 \text{ mAh g}^{-1}$  at 10 C), and a stable cyclic performance (85.2% of initial capacity after 1000 cycles). Given the simplicity and economy of the electrostatic self-assembly method, it can be broadly applicable across various technological domains.

## 2. Materials and Methods

### 2.1. Synthesis of Materials

Preparation of  $\text{Ti}_3\text{C}_2\text{T}_x$  suspension [40]: First, 1.6 g LiF (Macklin, AR) was mixed into a Teflon liner containing 20 mL of 9 mol L<sup>-1</sup> HCl and stirred at 45 °C for 15 min. An amount of 1 g  $\text{Ti}_3\text{AlC}_2$  powder (Jilin 11 Technology Co., Ltd., Changchun, China) was added slowly, and continuously stirred at 45 °C for 24 h. Then, the collected reaction products were washed with deionized water by repeated centrifugation (2000 rpm for 3 min) until pH = 6, hand-shaking for 5 min, and then centrifugation (2000 rpm for 10 min), repeated three times. The concentration of MXene was about 1 mg mL<sup>-1</sup> in the suspension.

Synthesis of NFPP@C [41,42]: 5.9994 g  $\text{Fe}(\text{NO}_3)_3 \cdot 9\text{H}_2\text{O}$  (Sinopharm, AR), 2.3996 g  $\text{NaH}_2\text{PO}_4 \cdot 2\text{H}_2\text{O}$  (Aladdin, AR), and 1.5118 g glucose (Sinopharm, AR) were dissolved in 50 mL deionized water (the molar ratio of  $\text{NaH}_2\text{PO}_4:\text{Fe}(\text{NO}_3)_3$  was 4:2.97), and then heated (80 °C) until the water evaporated completely, and the collected yellow xerogel and was ground. The resulting powder was calcined at 300 °C for 5 h and 550 °C for 10 h in a flowing N<sub>2</sub> atmosphere to obtain NFPP@C nanoparticles.

Preparation of NFPP@MX and NFPP/MX: To prepare NFPP@MX composite, 100 mg NFPP@C particles were added into 5 mL 1.2 mg mL<sup>-1</sup> CTAB ( $\text{C}_{19}\text{H}_{42}\text{BrN}$ , (Macklin, AR)) solution and stirred for 0.5 h. Then, this mixture was dropped into 5 mL  $\text{Ti}_3\text{C}_2\text{T}_x$  suspension and continuously stirred for 0.5 h. The mass of  $\text{Ti}_3\text{C}_2\text{T}_x$  was about 5 wt.% of NFPP@C. Subsequently, the black product was collected and washed several times to remove the residual CTAB, then dried overnight to obtain NFPP@MX powder. NFPP/MX composite was prepared in the same way as above, except that the CTAB aqueous solution was replaced with an equal amount of deionized water.

### 2.2. Material Characterization

X-ray diffraction (XRD) patterns of the samples were collected on a Malvern Panalytical Empyrean in the intervals from 5° to 85° (2θ) with a scanning speed of 5° min<sup>-1</sup>. The detailed morphology and elemental distribution of the samples were characterized using a transmission electron microscope (TEM, FEI Tecnai F20) and a scanning electron microscope with EDS mapping module (SEM, Hitachi SU8010). The X-ray photoelectron spectroscopy (XPS) measurements were carried out on a PHI500 spectrometer. Fourier transform infrared spectroscopy (FT-IR) spectra were examined via a Thermo Nicolet iS5 in the range of 4000–400 cm<sup>-1</sup> wave numbers. Thermogravimetric analysis (TG) was conducted in air from 50 to 800 °C at a heating rate of 10 °C min<sup>-1</sup>.

### 2.3. Electrochemical Test

All electrochemical characterization was performed at room temperature with CR2032 coin cells. The obtained active substances, carbon black and poly(-vinylidene fluoride) (PVDF), were mixed with a mass ratio of 7:2:1 to form a homogeneous slurry, in which PVDF pre-dispersed in N-methyl-2-pyrolidone (NMP). Later, the slurry was uniformly cast on Al foil and vacuum dried at 60 °C for 12 h. The electrode loading density was about 1.5 mg cm<sup>-2</sup>. NFPP@C, NFPP/MX, and NFPP@MX electrodes were employed as cathodes; sodium metal foils as reference electrodes. The electrolyte was 1 M NaClO<sub>4</sub> dissolved in propylene carbonate (PC) with 5 vol. % fluoroethylene carbonate (FEC). The separator was glass fiber (GF/D). The galvanostatic charge/discharge performance was measured on a CT2001A test system (Land Wuhan, China). Cyclic voltammetry (CV) curves and electrochemical impedance spectra (EIS) were recorded using a CHI660e (Shanghai, China). The test frequency range of EIS was 100 k~0.1 Hz. The full cells were assembled using NFPP@MX and commercial hard carbon (CHC). CHC anodes were first cycled 5 times in CHC//Na half cells and then charged to 1.2 V. All cell assembly/disassembly was performed in an Ar atmosphere. The charge/discharge capacity presented in this work is calculated based on the mass of NFPP@C in the sample.

### 3. Results and Discussion

Figure 1a schematically demonstrates the synthesis process of NFPP@MX composite. Upon treatment with HCl/LiF, the aluminum atomic layer located within the densely packed layered structure of commercial  $\text{Ti}_3\text{AlC}_2$  was selectively removed, leading to the formation of the accordion-like  $\text{Ti}_3\text{C}_2\text{T}_x$  (Figure S1). Then, the etched  $\text{Ti}_3\text{C}_2\text{T}_x$  was dispersed in water and a homogeneous  $\text{Ti}_3\text{C}_2\text{T}_x$  MXene colloidal solution was obtained via vigorous hand-shaking. Owing to the modification of the polar terminals ( $-\text{OH}$ ,  $-\text{O}$ , and  $-\text{F}$ ), the surface of the exfoliated  $\text{Ti}_3\text{C}_2\text{T}_x$  nanosheets is negatively charged. The electrostatic repulsion between the nanosheets makes the single-layer  $\text{Ti}_3\text{C}_2\text{T}_x$  stable in water (Figure 1b). CTAB is a common cationic surfactant. The NFPP@C particles were coated with  $\text{CTA}^+$  after continuous stirring. When the CTAB-modified NFPP@C particles (Figure 1c) were added into the  $\text{Ti}_3\text{C}_2\text{T}_x$  suspension, the  $\text{Ti}_3\text{C}_2\text{T}_x$  nanosheets were attracted to the surface of NFPP@C particles under electrostatic action. The complexes could be immediately observed settling to the bottom of the bottle if stirring was stopped (Figure 1d). In the absence of CTAB, the mixture of NFPP@C and  $\text{Ti}_3\text{C}_2\text{T}_x$  suspension was still black in the synthesis of NFPP/MX which means that  $\text{Ti}_3\text{C}_2\text{T}_x$  nanosheets cannot successfully be attracted to the surface of NFPP@C particles and single-layer  $\text{Ti}_3\text{C}_2\text{T}_x$  nanosheets still exist (Figure 1e). It is worth noting that a colloidal coagulation phenomenon occurred if CTAB solution was added into  $\text{Ti}_3\text{C}_2\text{T}_x$  suspension and shaken for a few seconds, because  $\text{CTA}^+$  neutralized the negative charge, reducing the repulsive forces between the nanosheets (Figure 1f). The above phenomenon proves that NFPP@C particles and  $\text{Ti}_3\text{C}_2\text{T}_x$  nanosheets can self-assemble with the assistance of CTAB. This process does not involve any thermal treatment and is very brief.

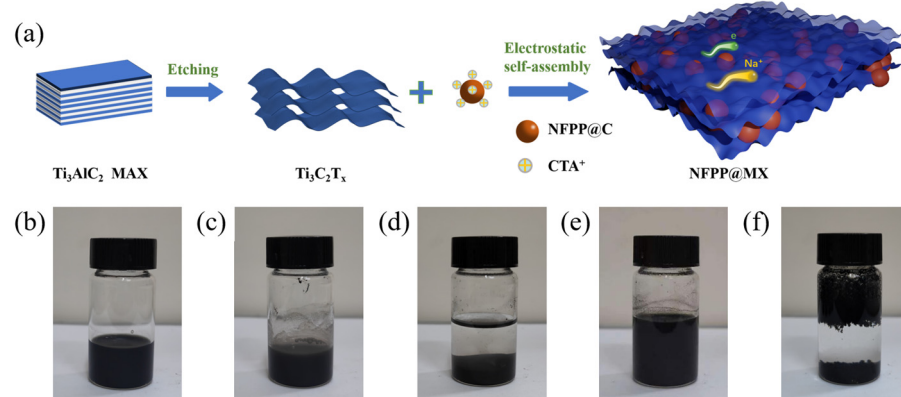


**Figure 1.** (a) Schematic illustration of the synthesis of NFPP@MX composite. (b) Optical image of  $\text{Ti}_3\text{C}_2\text{T}_x$  suspensions, (c) CTAB-modified NFPP@C, (d) NFPP@MX composite, (e) NFPP/MX composite, and (f) a mixture of CTAB solution and  $\text{Ti}_3\text{C}_2\text{T}_x$  suspensions.

The morphologies and microstructures of as-prepared NFPP@C, NFPP/MX, and NFPP@MX samples were investigated by SEM, TEM, and EDS. In Figure S2a, NFPP@C has a regular spherical particle structure and a particle size of 80–200 nm. The SEM images of the NFPP/MX composite (Figure S2b) depict the presence of both NFPP@C particles and planar  $\text{Ti}_3\text{C}_2\text{T}_x$  nanosheets. The finite and weak contact between NFPP@C particles and  $\text{Ti}_3\text{C}_2\text{T}_x$  nanosheets cannot effectively improve the conductivity of NFPP/MX composite, but in NFPP@MX samples, NFPP@C particles are embedded in a 3D structure composed of crumpled MXene nanosheets, and the increased contact area between particles significantly improves the electron transport efficiency.

The tight cross-linking between NFPP@C and MXene nanosheets is further demonstrated by the TEM images in Figure 2a,b. MXene nanosheets with large lattice stripes and NFPP particles form a compact structure, and the lattice fringes of the MXene sheets are about 1.5 nm. Figure 2c illustrates a lattice dimension of 0.26 nm, which is very close to

the interplanar spacing of (602) plane of the typical NFPP crystal [33]. Moreover, there is a 4.8 nm thick carbon layer on the surface of NFPP@C particles.

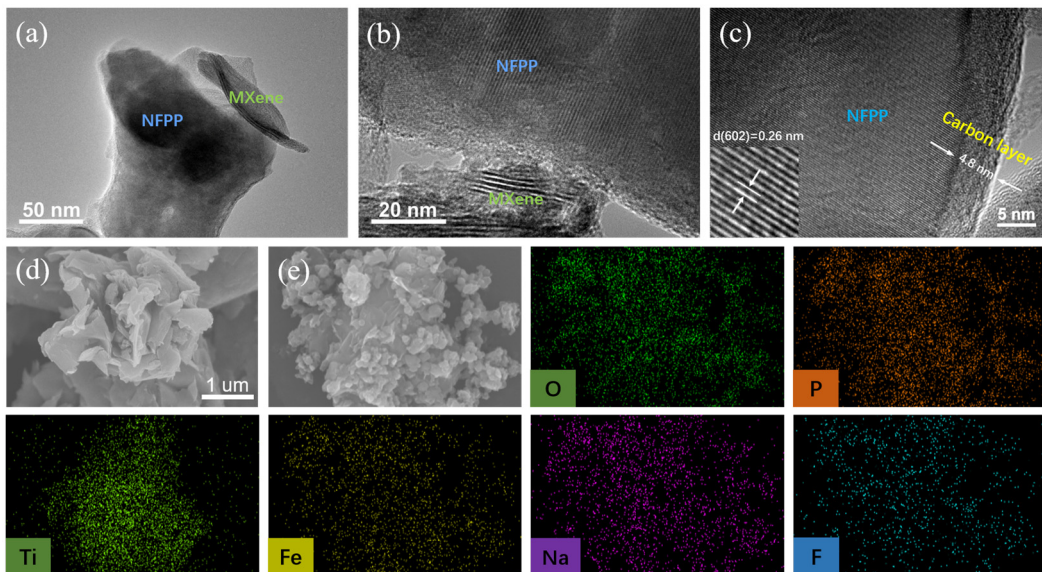


**Figure 2.** (a–c) TEM images of NFPP@MX. (d) SEM image of crumpled  $\text{Ti}_3\text{C}_2\text{T}_x$  nanosheets. (e) Typical SEM image of NFPP@MX and the corresponding elemental mappings.

The SEM image of crumpled  $\text{Ti}_3\text{C}_2\text{T}_x$  nanosheets obtained by mixing CTAB solution and  $\text{Ti}_3\text{C}_2\text{T}_x$  suspension (Figure 1e) is shown in Figure 2d. Compared with the flat microstructure of  $\text{Ti}_3\text{C}_2\text{T}_x$  nanosheets in NFPP/MX composite, it can be seen that CTAB can destroy the repulsion force between the nanosheets, resulting in a stacking and crumpled phenomenon of the  $\text{Ti}_3\text{C}_2\text{T}_x$  nanosheets. The feasibility of the electrostatic self-assembly method is further confirmed [43]. The EDS images in Figure 2e display a uniform distribution of Na, Fe, P, and O elements. Ti element is derived from  $\text{Ti}_3\text{C}_2\text{T}_x$  nanosheets and F element is also detected due to the presence of the surface termination (-F). The even distribution of elements indicates that the NFPP@C nanoparticles are effectively coated by  $\text{Ti}_3\text{C}_2\text{T}_x$  nanosheets.

The XRD pattern of NFPP@MX is depicted in Figure 3a, and its structural parameters were analyzed by GSASII software. The calculated diffraction patterns match well with the observed XRD patterns. Peaks at  $15.9^\circ$ ,  $16.7^\circ$ ,  $23.9^\circ$ ,  $25.9^\circ$ ,  $32.1^\circ$ ,  $33.7^\circ$ ,  $34.4^\circ$  can be indexed to the crystal planes of NFPP (011), (002), (410), (402), (022), (222), and (602), respectively. The analysis results reveal that NFPP belongs to the  $Pn21a$  space group and lattice parameters of  $a = 17.8603 \text{ \AA}$ ,  $b = 6.5015 \text{ \AA}$ ,  $c = 10.7283 \text{ \AA}$ , and  $V = 1245.75 \text{ \AA}^3$ ; maricite  $\text{NaFePO}_4$  impurity was also detected in the sample whose peaks locate at  $20.1^\circ$ ,  $32.8^\circ$ ,  $33.1^\circ$ ,  $34.8^\circ$ , respectively [44]. The weight fraction of maricite  $\text{NaFePO}_4$  is about 7% based on Rietveld XRD results. The diffraction peak at about  $8^\circ$  ( $2\theta$ ) corresponds to the characteristic (002) plane of  $\text{Ti}_3\text{C}_2\text{T}_x$ ; NFPP@C and NFPP@MX exhibit similar XRD profiles, and the diffraction peaks of  $\text{Ti}_3\text{C}_2\text{T}_x$  are not detected in the NFPP@MX composite, probably due to its low content (Figure S3). The FT-IR spectra of NFPP@C and NFPP@MX are displayed in Figure 3b; several peaks in the range  $400\text{--}700 \text{ cm}^{-1}$  are identified, which originate from the O-P-O bending vibrations, the mid-frequency peaks ( $718$  and  $956 \text{ cm}^{-1}$ ) are due to symmetric and antisymmetric vibrations of the  $\text{P}_2\text{O}_7$  groups, while the stretching mode of the P-O in  $\text{PO}_4$  groups produces the bulge at  $718\text{--}956 \text{ cm}^{-1}$  [45].

The structural characteristics and carbon layer components of NFPP@C and NFPP@MX were studied by Raman spectroscopy (Figure 3c), and the characteristic Raman fingerprint of NFPP is displayed in the band range of  $250$  to  $1100 \text{ cm}^{-1}$ . The multiple peaks in the low frequency region ( $<500 \text{ cm}^{-1}$ ) are associated with the deformation of the  $\text{PO}_4$  unit, while the strong peaks near  $1000 \text{ cm}^{-1}$  can be assigned to the stretching vibration of  $\text{PO}_4$

and  $\text{P}_2\text{O}_7$  [46]. Two distinct broad peaks at 1350 and 1580  $\text{cm}^{-1}$  belong to the D-band (disordered carbon) and G-band (graphitized carbon), respectively. The calculated relative intensities of NFPP@C and NFPP@MX in the D and G bands are 0.78 and 0.73, respectively, indicating that both samples have highly graphitized carbon layers. The small difference in  $I_{\text{D}}/I_{\text{G}}$  may be caused by the loss of a small amount of carbon during the preparation of NFPP@MX. XPS spectra were recorded to further investigate the product composition. The full XPS spectra confirm the existence of Ti, C, and O elements in NFPP@MX composite, which correspond well to the elemental composition of  $\text{Ti}_3\text{C}_2\text{T}_x$  (Figure S4a). The XPS result of C 1s in Figure 3d can be split into four main bonding configurations, namely C-Ti-Tx (281.8 eV), C-C (284.8 eV), C-O (286.2 eV), and O-C=O (288.3 eV) bonds. The binding energies of Ti 2p at 455 (461.1), 456 (461.8), 457.7 (463.6), and 459 (464.7) eV belong to Ti-C,  $\text{Ti}^{2+}$ ,  $\text{Ti}^{3+}$ , and  $\text{Ti}^{4+}$ -O bonds, respectively (Figure 3e) [47]. The XPS spectra of O 1s, P 1s, and Fe 2p are shown in Figure S4 [48]. Two distinct peaks are found at 711.2 eV ( $\text{Fe } 2\text{p}_{3/2}$ ) and 724.6 eV ( $\text{Fe } 2\text{p}_{1/2}$ ), indicating bivalent  $\text{Fe}^{2+}$  [49]. Furthermore, based on thermogravimetric (TG) analysis (Figure 3f), the calculated carbon content in NFPP@C is 5.9 wt.% (Note S1).

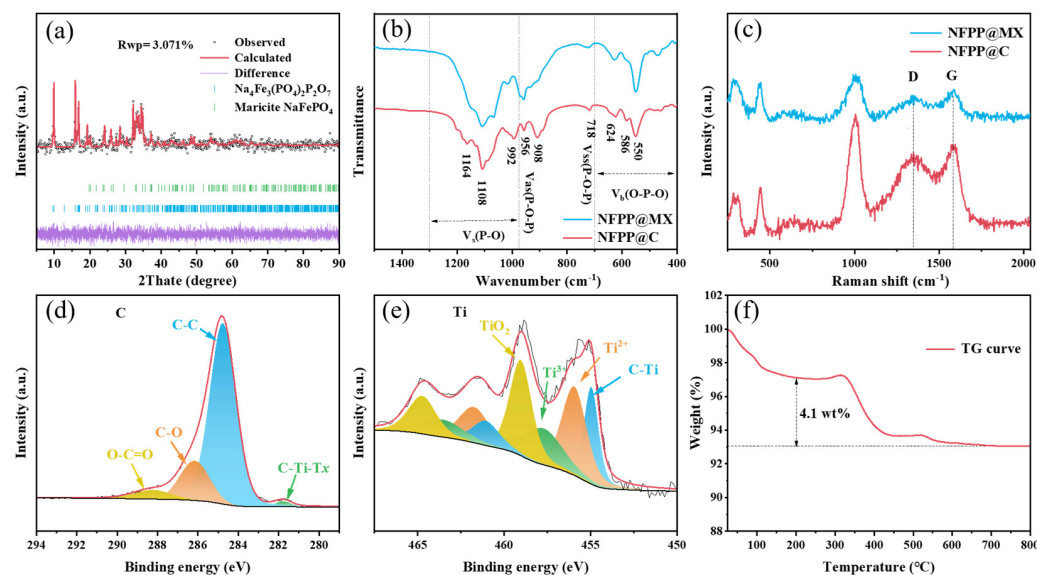


**Figure 3.** (a) Rietveld refinement of the XRD patterns of NFPP@MX. (b) FTIR spectra, and (c) Raman spectra of NFPP@C and NFPP@MX samples. XPS spectra of NFPP@MX composite in (d) C 1s region and (e) Ti 2p region. (f) TG curve of NFPP@C sample.

Electrochemical tests were carried out on half cells assembled with three materials. Figure 4a shows the CV curves of the NFPP@MX electrode at 0.1  $\text{mV s}^{-1}$ . Multiple anode and cathode peaks can be observed and they are not symmetric, which is correlated with the unique distribution of Na ions in NFPP crystals. Wu et al. demonstrated the existence of four Na sites with different coordination numbers in the NFPP crystal structure by using ex situ solid state NMR spectroscopy, namely Na3 (5-coordination), Na1 (6-coordination), Na4 (6-coordination), and Na2 (7-coordination) [31]. Among them, the 7-coordination Na2 is hardly involved in electrochemical reactions. Moreover, it is found that sodium ions with fewer coordination numbers are extracted first but inserted last. Therefore, during a complete charge and discharge process, the sodium ion extraction sequence is  $\text{Na}_3 \rightarrow \text{Na}_1 \rightarrow \text{Na}_4$ , while the insertion sequence is  $\text{Na}_4 \rightarrow \text{Na}_1 \rightarrow \text{Na}_3$ . In addition, the nearly coincident CV curves show that NFPP@MX has excellent reversibility.

Figure 4b presents the initial charge/discharge profiles of NFPP@C, NFPP/MX, and NFPP@MX cathodes at 0.2 C (1 C = 129  $\text{mA g}^{-1}$ ). All three materials have the same operating voltage platform in the range of 1.7–4 V, indicating the addition of  $\text{Ti}_3\text{C}_2\text{T}_x$  did not change the electrochemical properties of NFPP. Three charge voltage plateaus (2.90, 3.01, and 3.28 V) and two discharge voltage plateaus (3.17 and 2.81 V) can be observed,

which are in excellent agreement with the CV plots shown in Figure 4a. NFPP@MX delivers a discharge capacity of  $107.2 \text{ mAh g}^{-1}$  with an initial Coulombic efficiency of 98.7%, which is higher than those of NFPP/MX ( $105.1 \text{ mAh g}^{-1}$ , 97.4%) and NFPP@C ( $96.8 \text{ mAh g}^{-1}$ , 94.3%). The rate capabilities of the three electrodes are displayed in Figure 4c. The average reversible capacities of NFPP@MX are 106.1, 93.5, 86.1, 78.1, and  $70 \text{ mAh g}^{-1}$  obtained at 0.2, 0.5, 1, 2, and 5 C, respectively. NFPP/MX has discharge capacities of 104.8, 89, 79.4, 68.9, and  $56.7 \text{ mAh g}^{-1}$ , while those of the NFPP@C electrodes are only 97, 81.2, 71.9, 65.9, and  $53 \text{ mAh g}^{-1}$ . Notably, the NFPP@MX electrode maintains a reversible capacity of  $60.4 \text{ mAh g}^{-1}$  even at 10 C. NFPP/MX and NFPP@MX have similar capacities at low current, but NFPP@MX exhibits significantly higher capacities as the rate increases, which indicates the advantage of the crumpled MXene structure. We also tested long-term cycling at 0.5 C and 1 C to simulate real life. In Figure 4d, the capacity retention of NFPP@MX after 200 cycles is 97.4%, higher than those of NFPP/MX (92.8%) and NFPP@C electrodes (89.5%). When the current density is further increased to 1 C, the capacity retentions of NFPP@C and NFPP@MX after 1000 cycles are 68% and 85.2%, respectively. Both samples have excellent average coulomb efficiency (Figure 4e).

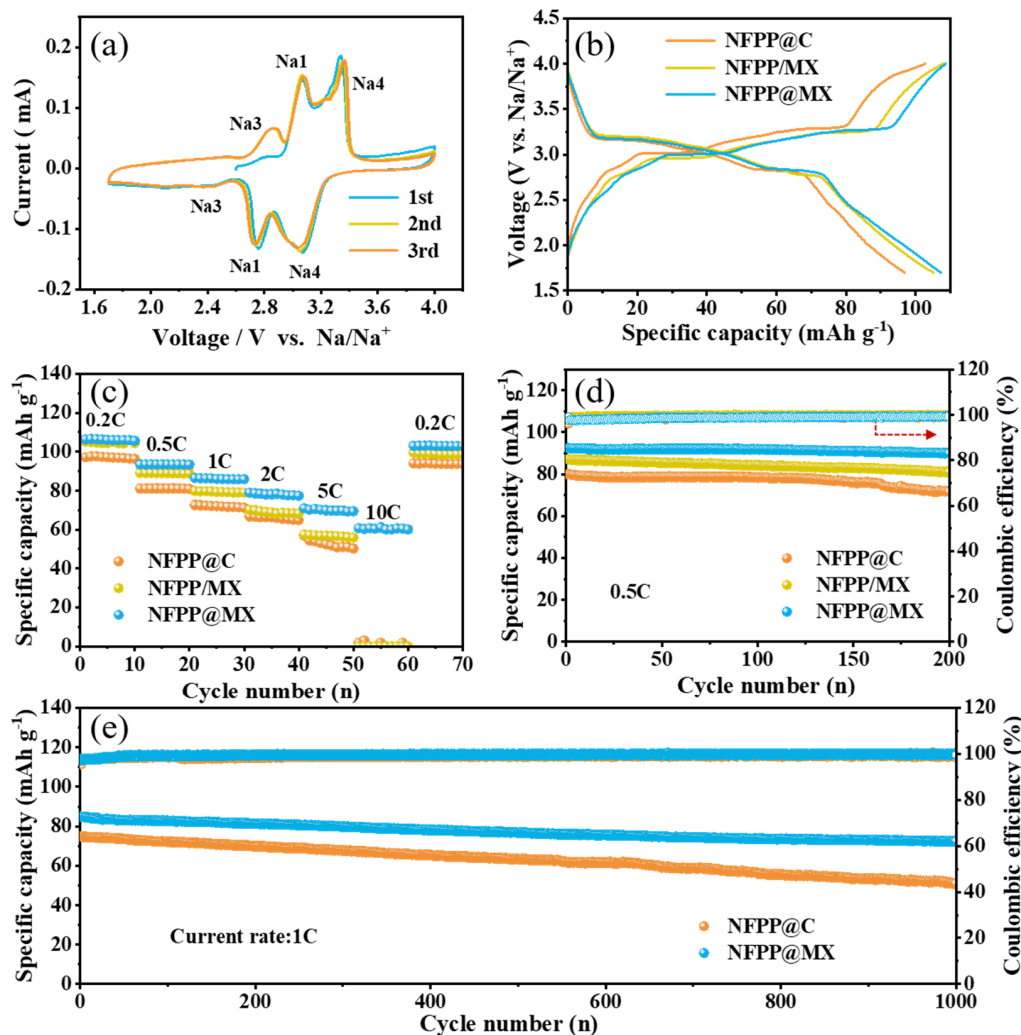


**Figure 4.** (a) Cyclic voltammetry (CV) curves of NFPP@MX at  $0.1 \text{ mV s}^{-1}$ . (b) Initial charge/discharge curves, (c) rate capability, and (d) cycling performance of NFPP@C, NFPP/MX, and NFPP@MX cathodes. (e) Long-term cycling performances of NFPP@C and NFPP@MX electrodes at 1 C.

Obviously, the NFPP@MX cathode exhibits better electrochemical performances compared to the other two electrodes. Compared with the finite connection area between

$\text{Ti}_3\text{C}_2\text{T}_x$  nanosheets and NFPP@C particles in the NFPP/MX sample, the 3D coupled structure in NFPP@MX expands the contact surface between particles which improves the conductivity of the electrode, resulting in higher discharge specific capacity. Besides acting as the external flexible skeleton of NFPP@C,  $\text{Ti}_3\text{C}_2\text{T}_x$  can effectively reduce the aggregation of NFPP@C particles and improve the structural stability of NFPP@MX electrodes during the charge and discharge process, thus achieving higher capacity retention. The electrochemical performances of cathode materials for Na-ion batteries are summarized and demonstrated in Table S3. As demonstrated, NFPP@MX cathode material exhibits relatively high capacity, excellent rate capability, and cycling stability.

To further study the difference in reaction kinetics between NFPP@C and NFPP@MX, CV curves of the both materials were tested between 0.05 and 0.2 mV s<sup>-1</sup> [50]. As presented in Figure 5a,b, the voltage gap between the oxidation and reduction peaks for NFPP@MX is smaller than that for NFPP@C as the scanning rate increases, indicating that NFPP@MX has better reversibility. The apparent diffusion coefficient of sodium ions ( $D$ ) can be calculated based on the Randles–Sevcik equation:

$$i_p = 2.69 \times 10^5 n^{2/3} A D^{1/2} C_0 v^{1/2}$$

where  $i_p$  is the peak current (A),  $n$  is the number of transferred electrons ( $n$  equals three for NFPP),  $A$  is the apparent electrode area (0.785 cm<sup>2</sup>),  $C_0$  is the bulk concentration of the  $\text{Na}^+$  in NFPP crystals ( $5.302 \times 10^{-3}$  mol cm<sup>-3</sup>), and  $v$  is the scan rate [51–53]. Figure 5c,d shows the linear fitting results of  $i_p$  and  $v^{1/2}$ . As shown in Figure 5e, the  $D$  values of the anodic (peak1, peak2) and cathodic peaks (peak3, peak4) of NFPP@MX cathodes are calculated as  $8.09 \times 10^{-12}$ ,  $1.79 \times 10^{-11}$ ,  $8.81 \times 10^{-12}$ , and  $9.7 \times 10^{-12}$  cm<sup>2</sup> s<sup>-1</sup>, respectively, which are significantly higher than those calculated for NFPP@C and NFPP/MX. The enhanced diffusion kinetics is correlated to the shorter diffusion pathways of sodium ions in NFPP@MX (Figure S5 and Table S1). The EIS spectra of the NFPP@C, NFPP/MX, and NFPP@MX cathodes are shown in Figure 5f. The semicircle at medium-high frequency indicates the charge transfer resistance ( $R_{ct}$ ) [54]. As shown in Table S2, NFPP@MX electrode has the smallest  $R_{ct}$  value (equivalent circuit shown in the inset of Figure 5f). These results show that the 3D crumpled  $\text{Ti}_3\text{C}_2\text{T}_x$  network can effectively improve the reaction kinetics of sodium ions.

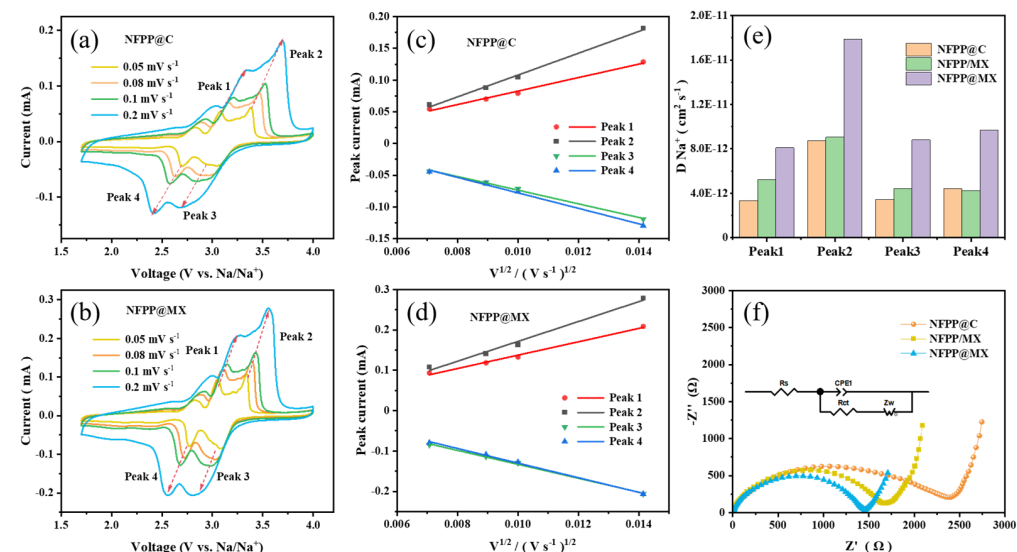


**Figure 5.** CV curves of (a) NFPP@C, (b) NFPP@MX cathodes at various scanning rates (0.05, 0.08, 0.1, and 0.2 mV s<sup>-1</sup>) and (c,d) corresponding relationships between the peak current and the square root of the scan rate. (e) The apparent diffusion coefficient of sodium ions of the three materials. (f) The EIS spectra of the three materials.

Commercial hard carbon (CHC) was selected as the anode to further test the performance of NFPP@MX in the full cell. The XRD pattern of CHC in Figure S6a has no obvious diffraction peak, which indicates that CHC is amorphous. The first discharge capacity of the CHC//Na half-cell is over  $700 \text{ mAh g}^{-1}$  at  $50 \text{ mA g}^{-1}$ , which is related to irreversible sodium loss in the formation of the SEI film. The CHC anode releases a capacity of  $247 \text{ mAh g}^{-1}$  during subsequent cycles, and most capacity is contributed by voltage plateaus  $<0.1 \text{ V}$  (Figure S6b). Figure 6a displays the first three charge/discharge profiles of the NFPP@MX full cell at  $0.2 \text{ C}$  during a voltage of  $1.0\text{--}4.0 \text{ V}$ . The full cell achieved a discharge capacity of  $95 \text{ mAh g}^{-1}$  and the initial coulombic efficiency was  $90.9\%$  (capacity is calculated based on cathode mass). Long-term cycling performances displayed in Figure 6b show that the NFPP@MX//CHC full cell has a first specific capacity of  $67.8 \text{ mA h g}^{-1}$  at  $1 \text{ C}$ , and maintain  $51 \text{ mA h g}^{-1}$  after  $100$  cycles.

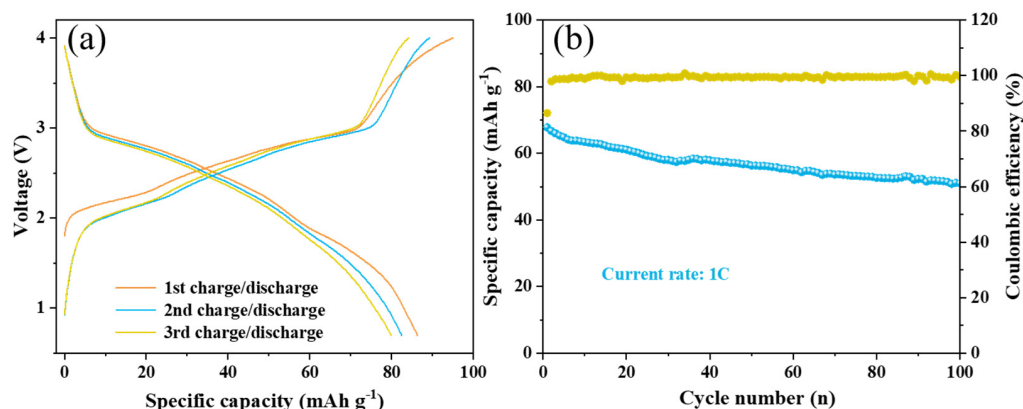


**Figure 6.** (a) The 1st–3rd charge/discharge curves at  $0.2 \text{ C}$  and (b) cyclic performance at  $1 \text{ C}$  of NFPP@MX//CHC full cell.

Therefore, it is expected that this crumpled  $\text{Ti}_3\text{C}_2\text{T}_x$  nanosheets construct plays a positive role in improving the electrochemical performances of NFPP@C cathode. First, the 3D crumpled structure provides “superhighways” for electron transportation. Second,  $\text{Ti}_3\text{C}_2\text{T}_x$  effectively prevents NFPP@C particles from aggregating, shortening diffusion pathways of sodium ions. Third,  $\text{Ti}_3\text{C}_2\text{T}_x$  nanosheets which exhibit excellent mechanical flexibility act as a flexible matrix to provide buffer space for the volume expansion of NFPP@C particles and enhance the structural stability of NFPP@MX electrodes during cycling.

#### 4. Conclusions

In summary, we successfully crumpled homogenous NFPP@C microspheres to a crumpled MXene conductive network by an electrostatic self-assembly process. This tightly cross-linked structure not only provides “superhighways” for fast electron transportation, but also acts as a positive restriction on the aggregation of NFPP@C particles and maintains fast sodium-ion diffusion. Consequently, NFPP@MX cathode exhibits a higher specific discharge capacity ( $106.1 \text{ mAh g}^{-1}$  at  $0.2 \text{ C}$ ,  $60.4 \text{ mAh g}^{-1}$  at  $10 \text{ C}$ ) and more stable cyclic performance ( $85.2\%$  of initial capacity after  $1000$  cycles) compared to NFPP@C cathode. Furthermore, sodium-ion fuel cells have been assembled and exhibit favorable cycling stability. Given the simplicity and economy of the electrostatic self-assembly method, we believe that it can be extended to other cathode modifications and NFPP@MX holds promising potential as a high-performance cathode material.

**Supplementary Materials:** The following supporting information can be downloaded at <https://www.mdpi.com/article/10.3390/batteries10040121/s1>: Figure S1: SEM images of (a)  $\text{Ti}_3\text{AlC}_2$  powders, and (b)  $\text{Ti}_3\text{C}_2\text{T}_x$  powders. Figure S2: SEM images of (a) NFPP@C, (b)NFPP/MX, and (c) NFPP@MX. Figure S3: XRD patterns of  $\text{Ti}_3\text{C}_2\text{T}_x$ , NFPP@C, and NFPP@MX. Figure S4: (a) Full XPS spectrum of NFPP@MX composite and corresponding XPS spectra of (b) O 1s region, (c) P 1s region,

(d) Fe 2p region. Figure S5: CV curves of (a) NFPP/MX cathodes at various scanning rates (0.05, 0.08, 0.1, and 0.2 mV s<sup>-1</sup>) and (b) corresponding relationships between  $i_p$  and  $v^{1/2}$ . Figure S6: (a) XRD pattern for CHC sample, (b) charge/discharge curves of CHC//Na half cells at 50 mA g<sup>-1</sup>. Note S1: Carbon content calculation process. Table S1: The calculated diffusion coefficients of the Na<sup>+</sup> ions ( $D$ ) of NFPP@C, NFPP/MX, and NFPP@MX. Table S2: Simulation results of the EIS spectra of three electrodes. Table S3: Comparison of cathode materials for Na-ion batteries [29,31,38,55–57].

**Author Contributions:** Conceptualization, A.X., Z.Y. and P.H.; methodology, A.X., D.S. and Z.Y.; validation, A.X., P.C. and Z.L.; formal analysis, D.S., Z.L. and Q.T.; investigation, D.L., X.Z., J.L. and Y.J.; data curation, A.X. and Z.Y.; writing—original draft preparation, A.X. and Z.Y.; writing—review and editing, Z.Y. and P.H.; supervision, Z.Y. and P.H.; project administration, Z.Y. and P.H.; funding acquisition, P.H. All authors have read and agreed to the published version of the manuscript.

**Funding:** This research received no external funding.

**Data Availability Statement:** The data presented in this study are available upon request from the corresponding author. The data are not publicly available due to privacy policy.

**Conflicts of Interest:** Authors Deyou Shi, Peng Chen, Zhongjun Li, and Quan Tu were employed by the company Wuhan Qina New Energy Technology Co., Ltd. The remaining authors declare that the research was conducted in the absence of any commercial or financial relationships that could be construed as a potential conflict of interest.

## References

1. Ayerbe, E.; Berecibar, M.; Clark, S.; Franco, A.A.; Ruhland, J. Digitalization of Battery Manufacturing: Current Status, Challenges, and Opportunities. *Adv. Energy Mater.* **2022**, *12*, 2102696. [[CrossRef](#)]
2. Fichtner, M.; Edström, K.; Ayerbe, E.; Berecibar, M.; Bhowmik, A.; Castelli, I.E.; Clark, S.; Dominko, R.; Erakca, M.; Franco, A.A.; et al. Rechargeable Batteries of the Future—The State of the Art from a BATTERY 2030+ Perspective. *Adv. Energy Mater.* **2022**, *12*, 2102904. [[CrossRef](#)]
3. Frith, J.T.; Lacey, M.J.; Ulissi, U. A non-academic perspective on the future of lithium-based batteries. *Nat. Commun.* **2023**, *14*, 420. [[CrossRef](#)] [[PubMed](#)]
4. Chen, M.; Hua, W.; Xiao, J.; Cortie, D.; Chen, W.; Wang, E.; Hu, Z.; Gu, Q.; Wang, X.; Indris, S.; et al. NASICON-type air-stable and all-climate cathode for sodium-ion batteries with low cost and high-power density. *Nat. Commun.* **2019**, *10*, 1408. [[CrossRef](#)] [[PubMed](#)]
5. Konarov, A.; Myung, S.-T.; Sun, Y.-K. Cathode Materials for Future Electric Vehicles and Energy Storage Systems. *ACS Energy Lett.* **2017**, *2*, 703–708. [[CrossRef](#)]
6. Vincent, M.; Kumar, S.S.; Kowalski, D. Pseudocapacitive vs diffusion controlled charge storage in Fe<sub>2</sub>O<sub>3</sub> nanosheet Na-ion battery. *Electrochim. Acta* **2023**, *469*, 143161. [[CrossRef](#)]
7. Rubio, S.; Maça, R.R.; Aragón, M.J.; Cabello, M.; Castillo-Rodríguez, M.; Lavela, P.; Tirado, J.L.; Etacheri, V.; Ortiz, G.F. Superior electrochemical performance of TiO<sub>2</sub> sodium-ion battery anodes in diglyme-based electrolyte solution. *J. Power Sources* **2019**, *432*, 82–91. [[CrossRef](#)]
8. Tian, Y.; Zeng, G.; Rutt, A.; Shi, T.; Kim, H.; Wang, J.; Koettgen, J.; Sun, Y.; Ouyang, B.; Chen, T.; et al. Promises and Challenges of Next-Generation “Beyond Li-ion” Batteries for Electric Vehicles and Grid Decarbonization. *Chem. Rev.* **2021**, *121*, 1623–1669. [[CrossRef](#)] [[PubMed](#)]
9. Wang, C.; Liu, L.; Zhao, S.; Liu, Y.; Yang, Y.; Yu, H.; Lee, S.; Lee, G.-H.; Kang, Y.-M.; Liu, R.; et al. Tuning local chemistry of P2 layered-oxide cathode for high energy and long cycles of sodium-ion battery. *Nat. Commun.* **2021**, *12*, 2256. [[CrossRef](#)]
10. Peng, J.; Zhang, W.; Liu, Q.; Wang, J.; Chou, S.; Liu, H.; Dou, S. Prussian Blue Analogues for Sodium-Ion Batteries: Past, Present, and Future. *Adv. Mater.* **2022**, *34*, 2108384. [[CrossRef](#)]
11. Hou, P.; Yin, J.; Lu, X.; Li, J.; Zhao, Y.; Xu, X. A stable layered P3/P2 and spinel intergrowth nanocomposite as a long-life and high-rate cathode for sodium-ion batteries. *Nanoscale* **2018**, *10*, 6671–6677. [[CrossRef](#)] [[PubMed](#)]
12. Yao, H.-R.; Wang, P.-F.; Gong, Y.; Zhang, J.; Yu, X.; Gu, L.; OuYang, C.; Yin, Y.-X.; Hu, E.; Yang, X.-Q.; et al. Designing Air-Stable O<sub>3</sub>-Type Cathode Materials by Combined Structure Modulation for Na-Ion Batteries. *J. Am. Chem. Soc.* **2017**, *139*, 8440–8443. [[CrossRef](#)] [[PubMed](#)]
13. Huang, X.; Zhang, W.; Zhou, C.; Yang, L.; Wang, H.; Gao, Q.; Zhu, M. N-doped carbon encapsulated CoMoO<sub>4</sub> nanorods as long-cycle life anode for sodium-ion batteries. *J. Colloid. Interface Sci.* **2020**, *576*, 176–185. [[CrossRef](#)]
14. Zhang, L.-L.; Wei, C.; Fu, X.-Y.; Chen, Z.-Y.; Yan, B.; Sun, P.-P.; Chang, K.-J.; Yang, X.-L. Ternary Ni-based Prussian blue analogue with superior sodium storage performance induced by synergistic effect of Co and Fe. *Carbon. Energy* **2021**, *3*, 827–839. [[CrossRef](#)]
15. Peng, J.; Zhang, W.; Hu, Z.; Zhao, L.; Wu, C.; Peleckis, G.; Gu, Q.; Wang, J.-Z.; Liu, H.K.; Dou, S.X.; et al. Ice-Assisted Synthesis of Highly Crystallized Prussian Blue Analogues for All-Climate and Long-Calendar-Life Sodium Ion Batteries. *Nano Lett.* **2022**, *22*, 1302–13102. [[CrossRef](#)] [[PubMed](#)]

16. Peng, J.; Ou, M.; Yi, H.; Sun, X.; Zhang, Y.; Zhang, B.; Ding, Y.; Wang, F.; Gu, S.; López, C.A.; et al. Defect-free-induced Na<sup>+</sup> disordering in electrode materials. *Energy Environ. Sci.* **2021**, *14*, 3130–3140. [[CrossRef](#)]
17. Nose, M.; Nakayama, H.; Nobuhara, K.; Yamaguchi, H.; Nakanishi, S.; Iba, H. Na<sub>4</sub>Co<sub>3</sub>(PO<sub>4</sub>)<sub>2</sub>P<sub>2</sub>O<sub>7</sub>: A novel storage material for sodium-ion batteries. *J. Power Sources* **2013**, *234*, 175–179. [[CrossRef](#)]
18. Zhu, C.; Song, K.; van Aken, P.A.; Maier, J.; Yu, Y. Carbon-Coated Na<sub>3</sub>V<sub>2</sub>(PO<sub>4</sub>)<sub>3</sub> Embedded in Porous Carbon Matrix: An Ultrafast Na-Storage Cathode with the Potential of Outperforming Li Cathodes. *Nano Lett.* **2014**, *14*, 2175–2180. [[CrossRef](#)] [[PubMed](#)]
19. Jiang, Y.; Zeng, L.; Wang, J.; Li, W.; Pan, F.; Yu, Y. A carbon coated NASICON structure material embedded in porous carbon enabling superior sodium storage performance: NaTi<sub>2</sub>(PO<sub>4</sub>)<sub>3</sub> as an example. *Nanoscale* **2015**, *7*, 14723–14729. [[CrossRef](#)]
20. Langrock, A.; Xu, Y.; Liu, Y.; Ehrman, S.; Manivannan, A.; Wang, C. Carbon coated hollow Na<sub>2</sub>FePO<sub>4</sub>F spheres for Na-ion battery cathodes. *J. Power Sources* **2013**, *223*, 62–67. [[CrossRef](#)]
21. Wang, P.-F.; You, Y.; Yin, Y.-X.; Guo, Y.-G. Layered Oxide Cathodes for Sodium-Ion Batteries: Phase Transition, Air Stability, and Performance. *Adv. Energy Mater.* **2018**, *8*, 1701912. [[CrossRef](#)]
22. Ge, P.; Li, S.; Shuai, H.; Xu, W.; Tian, Y.; Yang, L.; Zou, G.; Hou, H.; Ji, X. Ultrafast Sodium Full Batteries Derived from X—Fe (X = Co, Ni, Mn) Prussian Blue Analogs. *Adv. Mater.* **2019**, *31*, 1806092. [[CrossRef](#)]
23. Xu, J.; Gu, E.; Zhang, Z.; Xu, Z.; Xu, Y.; Du, Y.; Zhu, X.; Zhou, X. Fabrication of porous Na<sub>3</sub>V<sub>2</sub>(PO<sub>4</sub>)<sub>3</sub>/reduced graphene oxide hollow spheres with enhanced sodium storage performance. *J. Colloid. Interface Sci.* **2020**, *567*, 84–91. [[CrossRef](#)] [[PubMed](#)]
24. Wang, S.; Hu, L.; Li, X.; Qiu, D.; Qiu, S.; Zhou, Q.; Deng, W.; Lu, X.; Yang, Z.; Qiu, M.; et al. Carbon enhanced nucleophilicity of Na<sub>3</sub>V<sub>2</sub>(PO<sub>4</sub>)<sub>3</sub>: A general approach for dendrite-free zinc metal anodes. *J. Energy Chem.* **2024**, *91*, 203–212. [[CrossRef](#)]
25. Deng, C.; Zhang, S. 1D Nanostructured Na<sub>7</sub>V<sub>4</sub>(P<sub>2</sub>O<sub>7</sub>)<sub>4</sub>(PO<sub>4</sub>) as High-Potential and Superior-Performance Cathode Material for Sodium-Ion Batteries. *ACS Appl. Mater. Interfaces* **2014**, *6*, 9111–9117. [[CrossRef](#)] [[PubMed](#)]
26. Gezović, A.; Vujković, M.J.; Milović, M.; Grudić, V.; Dominko, R.; Mentus, S. Recent developments of Na<sub>4</sub>M<sub>3</sub>(PO<sub>4</sub>)<sub>2</sub>(P<sub>2</sub>O<sub>7</sub>) as the cathode material for alkaline-ion rechargeable batteries: Challenges and outlook. *Energy Storage Mater.* **2021**, *37*, 243–273. [[CrossRef](#)]
27. Chen, Y.; Dong, C.; Chen, L.; Fu, C.; Zeng, Y.; Wang, Q.; Cao, Y.; Chen, Z. “One stone two birds” design for hollow spherical Na<sub>4</sub>Fe<sub>3</sub>(PO<sub>4</sub>)<sub>2</sub>P<sub>2</sub>O<sub>7</sub>/C cathode enabled high-performance sodium-ion batteries from iron rust. *EcoMat* **2023**, *5*, e12393. [[CrossRef](#)]
28. Pu, X.; Wang, H.; Yuan, T.; Cao, S.; Liu, S.; Xu, L.; Yang, H.; Ai, X.; Chen, Z.; Cao, Y. Na<sub>4</sub>Fe<sub>3</sub>(PO<sub>4</sub>)<sub>2</sub>P<sub>2</sub>O<sub>7</sub>/C nanospheres as low-cost, high-performance cathode material for sodium-ion batteries. *Energy Storage Mater.* **2019**, *22*, 330–336. [[CrossRef](#)]
29. Cao, Y.; Xia, X.; Liu, Y.; Wang, N.; Zhang, J.; Zhao, D.; Xia, Y. Scalable synthesizing nanospherical Na<sub>4</sub>Fe<sub>3</sub>(PO<sub>4</sub>)<sub>2</sub>(P<sub>2</sub>O<sub>7</sub>) growing on MCNTs as a high-performance cathode material for sodium-ion batteries. *J. Power Sources* **2020**, *461*, 228130. [[CrossRef](#)]
30. Kim, H.; Park, I.; Seo, D.-H.; Lee, S.; Kim, S.-W.; Kwon, W.J.; Park, Y.-U.; Kim, C.S.; Jeon, S.; Kang, K. New Iron-Based Mixed-Polyanion Cathodes for Lithium and Sodium Rechargeable Batteries: Combined First Principles Calculations and Experimental Study. *J. Am. Chem. Soc.* **2012**, *134*, 10369–10372. [[CrossRef](#)]
31. Wu, X.; Zhong, G.; Yang, Y. Sol-gel synthesis of Na<sub>4</sub>Fe<sub>3</sub>(PO<sub>4</sub>)<sub>2</sub>(P<sub>2</sub>O<sub>7</sub>)/C nanocomposite for sodium ion batteries and new insights into microstructural evolution during sodium extraction. *J. Power Sources* **2016**, *327*, 666–674. [[CrossRef](#)]
32. Zhang, J.; Tang, L.; Zhang, Y.; Li, X.; Xu, Q.; Liu, H.; Ma, Z.-F. Polyvinylpyrrolidone assisted synthesized ultra-small Na<sub>4</sub>Fe<sub>3</sub>(PO<sub>4</sub>)<sub>2</sub>(P<sub>2</sub>O<sub>7</sub>) particles embedded in 1D carbon nanoribbons with enhanced room and low temperature sodium storage performance. *J. Power Sources* **2021**, *498*, 229907. [[CrossRef](#)]
33. Ma, X.; Wu, X.; Shen, P. Rational Design of Na<sub>4</sub>Fe<sub>3</sub>(PO<sub>4</sub>)<sub>2</sub>(P<sub>2</sub>O<sub>7</sub>) Nanoparticles Embedded in Graphene: Toward Fast Sodium Storage Through the Pseudocapacitive Effect. *ACS Appl. Energy Mater.* **2018**, *1*, 6268–6278. [[CrossRef](#)]
34. Wang, C.; Pan, Z.; Chen, H.; Pu, X.; Chen, Z. MXene-based materials for multivalent metal-ion batteries. *Batteries* **2023**, *9*, 174. [[CrossRef](#)]
35. Li, Y.; Zhu, Q.; Xu, M.; Zang, B.; Wang, Y.; Xu, B. Cu-Modified Ti<sub>3</sub>C<sub>2</sub>Cl<sub>2</sub> MXene with Zincophilic and Hydrophobic Characteristics as a Protective Coating for Highly Stable Zn Anode. *Adv. Funct. Mater.* **2023**, *33*, 2213416. [[CrossRef](#)]
36. Xu, W.; Liao, X.; Xu, W.; Zhao, K.; Yao, G.; Wu, Q. Ion Selective and Water Resistant Cellulose Nanofiber/MXene Membrane Enabled Cycling Zn Anode at High Currents. *Adv. Energy Mater.* **2023**, *13*, 2300283. [[CrossRef](#)]
37. Xu, E.; Zhang, Y.; Wang, H.; Zhu, Z.; Quan, J.; Chang, Y.; Li, P.; Yu, D.; Jiang, Y. Ultrafast kinetics net electrode assembled via MoSe<sub>2</sub>/MXene heterojunction for high-performance sodium-ion batteries. *Chem. Eng. J.* **2020**, *385*, 123839. [[CrossRef](#)]
38. Yue, L.; Wang, J.; Li, M.; Qin, J.; Cao, M. Conductive Ti<sub>3</sub>C<sub>2</sub>T<sub>x</sub> networks to optimize Na<sub>3</sub>V<sub>2</sub>O<sub>2</sub>(PO<sub>4</sub>)<sub>2</sub>F cathodes for improved rate capability and low-temperature operation. *Dalton Trans.* **2023**, *52*, 4717–4727. [[CrossRef](#)]
39. Chun, J.; Wang, X.; Wei, C.; Wang, Z.; Zhang, Y.; Feng, J. Flexible and free-supporting Prussian blue analogs/MXene film for high-performance sodium-ion batteries. *J. Power Sources* **2023**, *576*, 233165. [[CrossRef](#)]
40. Tian, Y.; An, Y.; Wei, C.; Xi, B.; Xiong, S.; Feng, J.; Qian, Y. Flexible and Free-Standing Ti<sub>3</sub>C<sub>2</sub>T<sub>x</sub> MXene@Zn Paper for Dendrite-Free Aqueous Zinc Metal Batteries and Nonaqueous Lithium Metal Batteries. *ACS Nano* **2019**, *13*, 11676–11685. [[CrossRef](#)]
41. Zhao, A.; Yuan, T.; Li, P.; Liu, C.; Cong, H.; Pu, X.; Chen, Z.; Ai, X.; Yang, H.; Cao, Y. A novel Fe-defect induced pure-phase Na<sub>4</sub>Fe<sub>2.91</sub>(PO<sub>4</sub>)<sub>2</sub>P<sub>2</sub>O<sub>7</sub> cathode material with high capacity and ultra-long lifetime for low-cost sodium-ion batteries. *Nano Energy* **2022**, *91*, 106680. [[CrossRef](#)]
42. Gezović, A.; Milović, M.; Bajuk-Bogdanović, D.; Grudić, V.; Dominko, R.; Mentus, S.; Vujković, M.J. An effective approach to reaching the theoretical capacity of a low-cost and environmentally friendly Na<sub>4</sub>Fe<sub>3</sub>(PO<sub>4</sub>)<sub>2</sub>(P<sub>2</sub>O<sub>7</sub>) cathode for Na-ion batteries. *Electrochim. Acta* **2024**, *476*, 143718. [[CrossRef](#)]

43. Wei, C.; Fei, H.; An, Y.; Zhang, Y.; Feng, J. Crumpled  $Ti_3C_2T_x$  (MXene) nanosheet encapsulated  $LiMn_2O_4$  for high performance lithium-ion batteries. *Electrochim. Acta* **2019**, *309*, 362–370. [[CrossRef](#)]
44. Kim, J.; Seo, D.-H.; Kim, H.; Park, I.; Yoo, J.-K.; Jung, S.-K.; Park, Y.-U.; Goddard III, W.A.; Kang, K. Unexpected discovery of low-cost maricite  $NaFePO_4$  as a high-performance electrode for Na-ion batteries. *Energy Environ. Sci.* **2015**, *8*, 540–545. [[CrossRef](#)]
45. Yuan, T.; Wang, Y.; Zhang, J.; Pu, X.; Ai, X.; Chen, Z.; Yang, H.; Cao, Y. 3D graphene decorated  $Na_4Fe_3(PO_4)_2(P_2O_7)$  microspheres as low-cost and high-performance cathode materials for sodium-ion batteries. *Nano Energy* **2019**, *56*, 160–168. [[CrossRef](#)]
46. Ma, X.; Pan, Z.; Wu, X.; Shen, P.K.  $Na_4Fe_3(PO_4)_2(P_2O_7)$ @ $NaFePO_4$ @C core-double-shell architectures on carbon cloth: A high-rate, ultrastable, and flexible cathode for sodium ion batteries. *Chem. Eng. J.* **2019**, *365*, 132–141. [[CrossRef](#)]
47. Shah, S.A.; Habib, T.; Gao, H.; Gao, P.; Sun, W.; Green, M.J.; Radovic, M. Template-free 3D titanium carbide ( $Ti_3C_2T_x$ ) MXene particles crumpled by capillary forces. *Chem. Commun.* **2017**, *53*, 400–403. [[CrossRef](#)]
48. He, J.; Tao, T.; Yang, F.; Sun, Z.; Huang, H. Phase-manipulated hierarchically core-shell  $Na_3(VO_{1-x}PO_4)2F_{1+2x}$  ( $0 \leq x \leq 1$ )@ $Na_3V_2(PO_4)_3$  and its synergistic effect with conformally wrapped reduced graphene oxide framework towards high-performance cathode for sodium-ion batteries. *Mater. Today Phys.* **2022**, *27*, 100813. [[CrossRef](#)]
49. Wang, X.; Feng, Z.; Huang, J.; Deng, W.; Li, X.; Zhang, H.; Wen, Z. Graphene-decorated carbon-coated  $LiFePO_4$  nanospheres as a high-performance cathode material for lithium-ion batteries. *Carbon* **2018**, *127*, 149–157. [[CrossRef](#)]
50. Pu, X.; Zhao, D.; Fu, C.; Chen, Z.; Cao, S.; Wang, C.; Cao, Y. Understanding and Calibration of Charge Storage Mechanism in Cyclic Voltammetry Curves. *Angew. Chem. Int. Ed.* **2021**, *60*, 21310–21318. [[CrossRef](#)]
51. Das, S.R.; Majumder, S.B.; Katiyar, R.S. Kinetic analysis of the  $Li^+$  ion intercalation behavior of solution derived nano-crystalline lithium manganate thin films. *J. Power Sources* **2005**, *139*, 261–268. [[CrossRef](#)]
52. Wang, N.; Wang, R.; Jiang, M.; Zhang, J. Electrochemical properties of mixed-phosphates  $Na_{x+2}Fe_{x+1}(PO_4)_x(P_2O_7)$  with different ratios of  $PO_4^{3-}/P_2O_7^{4-}$ . *J. Alloys Compd.* **2021**, *870*, 159382. [[CrossRef](#)]
53. Yang, Z.; Jiang, Y.; Xu, H.-H.; Huang, Y.-H. High-performance porous nanoscaled  $LiMn_2O_4$  prepared by polymer-assisted sol-gel method. *Electrochim. Acta* **2013**, *106*, 63–68. [[CrossRef](#)]
54. Wang, S.-B.; Ran, Q.; Yao, R.-Q.; Shi, H.; Wen, Z.; Zhao, M.; Lang, X.-Y.; Jiang, Q. Lamella-nanostructured eutectic zinc-aluminum alloys as reversible and dendrite-free anodes for aqueous rechargeable batteries. *Nat. Commun.* **2020**, *11*, 1634. [[CrossRef](#)] [[PubMed](#)]
55. Kadam, S.; Kate, R.; Chothe, U.; Chalwadi, P.; Shingare, J.; Kulkarni, M.; Kalubarme, R.; Kale, B. Highly Stable MWCNT@NVP Composite as a Cathode Material for Na-Ion Batteries. *ACS Appl. Mater. Interfaces* **2023**, *15*, 34651–34661. [[CrossRef](#)]
56. Zhu, Y.; Song, K.; Shen, S.; Liu, Z.; Xu, J.; Yang, L.; Zhao, L. Realizing efficient sodium storage property with NASICON-type  $Na_2VTi(PO_4)_3$  modified by nitrogen and sulfur dual-doped carbon layer for sodium ion batteries. *J. Alloys Compd.* **2021**, *856*, 157992. [[CrossRef](#)]
57. Li, J.; Wang, R.; Zhao, W.; Hou, X.; Paillard, E.; Ning, D.; Li, C.; Wang, J.; Xiao, Y.; Winter, M.; et al. A high-voltage symmetric sodium ion battery using sodium vanadium pyrophosphate with superior power density and long lifespan. *J. Power Sources* **2021**, *507*, 230183. [[CrossRef](#)]

**Disclaimer/Publisher’s Note:** The statements, opinions and data contained in all publications are solely those of the individual author(s) and contributor(s) and not of MDPI and/or the editor(s). MDPI and/or the editor(s) disclaim responsibility for any injury to people or property resulting from any ideas, methods, instructions or products referred to in the content.